








RESEARCH ARTICLE | NOVEMBER 11 2024

Modification of wind turbine wakes by large-scale, convective atmospheric boundary layer structures

Special Collection: [Preparatory work for the American Wake Experiment \(AWAKEN\)](#)

Lawrence Cheung ; Gopal Yalla ; Kenneth Brown ; Nathaniel deVelder; Alan Hsieh ; Thomas Herges; Daniel Houck ; David Maniaci; Philip Sakievich ; Aliza Abraham 



J. Renewable Sustainable Energy 16, 063304 (2024)
<https://doi.org/10.1063/5.0211722>



Articles You May Be Interested In

Probing the atmospheric boundary layer with integrated remote-sensing platforms during the American WAKE Experiment (AWAKEN) campaign

J. Renewable Sustainable Energy (November 2024)

Large eddy simulation of atmospheric boundary layer flow over complex terrain in comparison with RANS simulation and on-site measurements under neutral stability condition

J. Renewable Sustainable Energy (March 2023)

Toward understanding waked flow fields behind a wind turbine using proper orthogonal decomposition

J. Renewable Sustainable Energy (March 2021)



Special Topics Open for Submissions

[Learn More](#)

Modification of wind turbine wakes by large-scale, convective atmospheric boundary layer structures



Cite as: J. Renewable Sustainable Energy **16**, 063304 (2024); doi: 10.1063/5.0211722

Submitted: 1 April 2024 · Accepted: 27 September 2024 ·

Published Online: 11 November 2024



View Online



Export Citation



CrossMark

Lawrence Cheung,^{1,a)} Gopal Yalla,² Kenneth Brown,² Nathaniel deVelder,² Alan Hsieh,² Thomas Herges,² Daniel Houck,² David Maniaci,² Philip Sakievich,² and Aliza Abraham³

AFFILIATIONS

¹Sandia National Laboratories, Livermore, California 94550, USA

²Sandia National Laboratories, Albuquerque, New Mexico 87185, USA

³National Renewable Energy Laboratory, Golden, Colorado 80401, USA

Note: This article is part of the special issue Preparatory Work for the American Wake Experiment (AWAKEN).

^{a)}Author to whom correspondence should be addressed: lcheung@sandia.gov

ABSTRACT

In this study, we consider the impact of large-scale, convective structures in an unstable atmospheric boundary layer on wind turbine wakes. Simulation data from a high-fidelity large-eddy simulation (LES) of the AWAKEN wind farm site matching unstable atmospheric conditions were analyzed, and both turbine performance and wake behavior were affected based on their location relative to the convective structures. Turbines located in updraft regions of the flow experienced lower inflow velocity and generated less power, but their wakes were observed to recover faster and saw greater turbulent kinetic energy mixing higher in the boundary layer. The opposite effect was found for turbines in the downdraft regions of the convective structures. A simplified model of this wake behavior was also developed based on a two-dimensional $k-\epsilon$ Reynolds-Averaged Navier–Stokes formulation. This simplified model included the effects of vertical transport, but could be efficiently solved as a parabolic system, and was found to capture similar wake modifications observed in the high-fidelity LES computations.

© 2024 Author(s). All article content, except where otherwise noted, is licensed under a Creative Commons Attribution-NonCommercial-NoDerivs 4.0 International (CC BY-NC-ND) license (<https://creativecommons.org/licenses/by-nc-nd/4.0/>). <https://doi.org/10.1063/5.0211722>

I. INTRODUCTION

The current trend of deploying increasingly larger wind turbines along with more massive wind farm installations has introduced new challenges in predicting the performance of wind farms and understanding their interactions with the surrounding atmosphere. Of particular importance is understanding how complex atmospheric conditions can impact wind turbine and wind farm wakes, which directly affect the energy available to downstream installations. While it is well known that the overall atmospheric stability can strongly affect wind turbine wake behavior, the presence of large-scale convective structures in the atmospheric boundary layer (ABL) can also act to modify wake behavior. These large-scale structures, typically seen in unstable atmospheric conditions, can appear as convective rolls or long, coherent streaks with vertical updrafts and downdrafts and are associated with regions of lower- and higher-velocity flow, respectively. These large-scale structures in the ABL have been well studied in the literature^{1–3} including experimental observations^{4,5} and computational simulations.^{6,7}

Previous studies on wind turbine wake behavior under different atmospheric stability conditions have focused on the differences in overall behavior of the wakes between stable, neutral, and unstable boundary layers.^{8,9} For unstable conditions, fewer studies have focused on the interactions of large-scale convective structures with wind turbines, and many questions still remain regarding impacts of these structures on the operation of wind farms. Many turbine quantities, such as the generator power or damage equivalent loads, scale nonlinearly with the incoming wind speed, so these quantities depend on both the mean and fluctuating part of the wind speed. This means that in a flow with many high-speed and low-speed streaks, the time-averaged hub-height wind speed in a flow may eventually converge to a mean value, but the overall mean wind speed may not provide the full picture of the wind farm performance. Local variations in the flow field due to highly unstable atmospheric conditions can, thus, play a large role in the operation of wind farms.

The ongoing American WAKE experiment (AWAKEN) project¹⁰ is an opportunity to examine this phenomenon and answer these

questions. The data gathered from this field campaign allow researchers to study individual turbine wake behavior and larger scale farm wakes, as well as their interactions with dynamic atmospheric events. The deployed instrumentation at the AWAKEN sites is centered near five wind farms in northern Oklahoma and range from dual-Doppler radar, forward- and rear-facing turbine-mounted lidars, ground-based scanning and profiling lidars, as well as surface meteorological stations and airborne atmospheric measurements. Concurrent high-fidelity simulations^{11,12} in the AWAKEN project also supplement the gathered data and allow researchers to validate the outputs of various computational models against field measurements.

The result of such measurements and comparisons will ultimately lead to a better understanding of turbine wake behavior in complex environments as well as improvements in existing wake models. The updrafts and downdrafts caused by these structures can modify the wake properties beyond what can be predicted by current wake models.¹³ A relatively common characteristic of current wake models is the assumption of a steady inflow profile or the presence of neutral ABL conditions with negligible vertical velocity. For analytical wake models, such as the Jensen model¹⁴ or Gaussian velocity models,^{15,16} this simplification allows for very fast predictions of the wake properties but requires properly adjusted calibration parameters to handle different atmospheric conditions.

The use of the Reynolds-averaged Navier–Stokes (RANS) equations is a possible alternative to analytical wake models. RANS-based formulations allow for multiple turbine wakes in various conditions to be evaluated without incurring the expense of higher-fidelity large-eddy simulations (LES). This approach was demonstrated by Ainslie¹⁷ who used an axisymmetric formulation to derive a parabolic system that can be efficiently evolved in space. Such an approach was also considered by Iungo *et al.*¹⁸ who calibrated a mixing-length eddy-viscosity model to handle turbulent inflow conditions. Other developments have included WakeBlaster, a fully three-dimensional (3D) RANS model by Bradstock and Schlez¹⁹ to allow the wake model to capture inflow shear effects, and a depth-averaged RANS model by Letizia and Iungo²⁰ that was calibrated using lidar data from operational wind farms. More recent studies have examined solutions of the linearized RANS equations through the curled wake model,²¹ and fully 3D RANS models²² that model both the ABL inflow and the turbine wake under neutral and stable atmospheric conditions. However, the use of mid-fidelity RANS to model the impact of updraft and downdrafts on turbine wakes has not been well studied and may be important to consider. Including the capability to model the updraft and downdraft effects in a relatively simple formulation would lead to improvements in wind farm siting and turbine performance predictions.

In this work, we consider the effect of unstable atmospheric conditions on the behavior of wind turbine wakes using high-fidelity numerical simulations and a simplified wake model. The results of an LES wind farm simulation matching measured conditions at the AWAKEN site are discussed first in Sec. II. The updraft and downdraft flows associated with the convective structures are shown to have different impacts on the downstream wind turbine wake mixing evolution as well as the interaction of the wakes with the ABL. In addition, we present a simplified model of wake evolution based on the boundary layer RANS equations in Sec. III. These RANS equations are formulated to efficiently solve for the velocity profiles in the streamwise and vertical directions but also include the buoyancy and vertical

transport terms. The resulting wake profiles are then qualitatively compared with the LES observations. Finally, the conclusions and recommendations for future studies are presented in Sec. IV.

II. LARGE-EDDY SIMULATION AND WAKE RESULTS

A. Measured atmospheric conditions

One of the initial tasks in the AWAKEN project was to analyze the atmospheric characteristics near the wind farm sites and determine the prevalent wind conditions. Measurements at the nearby central C1 location of the Atmospheric Radiation Measurement (ARM) Climate Research Facility²³ were collected and analyzed over a 5-year period from January 2015 to November 2020. The wind speed, shear, turbulence, and surface meteorological characteristics were divided into stable, neutral, and unstable atmospheric stability states and the predominant conditions in each category were determined. Of particular interest to the current study are the unstable ABL conditions reported in Table I, which were chosen as the target conditions to replicate in the LES.

Additional insight into the structure of the unstable ABL can be found from dual-Doppler radar measurements at the AWAKEN site. These measurements were performed with two X-band radars from Texas Tech University.²⁴ The system offers volumetric measurements of horizontal wind velocity with the data interpolated to a horizontal grid of 25–50 m resolution at vertical intervals of 25 m every approximately 124 s, and uncertainty estimates are provided in Brown *et al.*²⁵ Notably, these instruments allowed for an unparalleled view of large-scale atmospheric structures across a swath of land larger than 700 km². Figure 1 shows two flow snapshots at 450 m above mean sea level (i.e., at a height intersecting the top half of the rotor planes of the turbines). The snapshots, which were taken during convectively unstable ABL conditions (as verified by a nearby surface meteorological station) on the afternoon and evening of September 24, 2023, indicate the presence of large atmospheric rolls and convective streaks aligned with the wind direction of roughly 67°. These rolls are comparable to the rolls observed in the LES described herein (see Fig. 2).

B. Computational methodology and simulation setup

Once the desired atmospheric conditions were determined, an equivalent simulation of the entire AWAKEN site and its wind farms was performed using LES. In this study, the ExaWind/AMR-Wind²⁶ solver was used to efficiently perform the computation on large-scale computing platforms. A short summary of the solver and the simulation setup is provided in the following paragraphs while a more complete description can be found in the earlier study by Cheung *et al.*¹¹

TABLE I. Median measured unstable ABL conditions from the ARM central facility from 2015 to 2020.

Parameter	Measurement height (m)	Median value
Wind speed	91	9.0 m/s
Wind direction	91	175°
Wind shear exponent	10–169	0.0898
Turbulence intensity	60	18.04%
Potential temperature	3	305.803 K

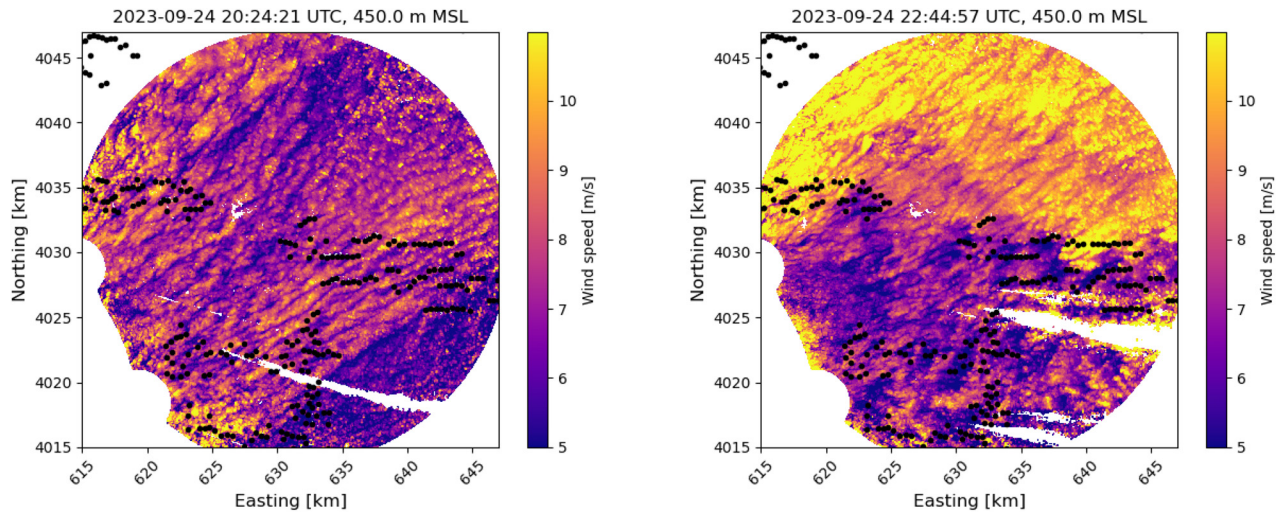


FIG. 1. Dual-Doppler radar flow snapshots over the measurement domain during convectively unstable ABL conditions at the AWAKEN domain with wind from the Northeast. The black circles indicate wind turbines from the King Plains, Breckenridge, and Armadillo Flats wind plants. The local times of these snapshots were 15:24 and 17:44 on September 24, 2023, when the sunset occurred at 19:26.

AMR-Wind solves the incompressible Navier–Stokes equations using a block-structured refinement algorithm. Additionally, scalar transport equations can be solved, such as potential temperature or turbulent kinetic energy. The discretization in AMR-Wind is based on the approximate projection method used in IAMR²⁷ and incflo.²⁸ It is a semi-staggered scheme in which the velocity and scalar variables are located at cell centers and pressure is located at nodes. Pressure is also staggered in time so that pressure and the pressure gradient are recorded at time $n + 1/2$. The time discretization is handled with a Crank Nicolson approach, and the advection term is handled explicitly using an upwind finite-volume method using the WENO-Z algorithm, leading to a method which is second-order accurate in both space and time.²⁹ For the simulations in this paper, we use an implicit scheme for the viscous terms and a second-order central difference scheme for the

diffusion terms. After the scalar equations and the momentum equations are advanced in time, a nodal projection is used to approximately correct the velocity field to make it divergence-free. Additional details on the AMR-Wind solver and its application to wind turbine simulations and wind farm applications are given by Sharma *et al.*³⁰ as well as Cheung *et al.*³¹

The computational domain encompassed the entire AWAKEN site spanning a $100 \times 100 \times 2.5 \text{ km}^3$ region using a background mesh resolution of 20 m that was successively refined to 2.5 m near the turbine rotor disks for a total of 21.14×10^9 mesh elements. The simulations were run on the Summit high-performance computing cluster at the Oak Ridge Leadership Computing Facility using 6000 GPUs and more than 1×10^6 GPU-hours. All simulations included both the Coriolis forcing term and the Boussinesq buoyancy model to capture the effects of wind veer and atmospheric stratification. Terrain effects were not included in these simulations, and a flat lower surface with the wall model of Moeng³² was used.

An initial precursor calculation without turbines was performed to allow the unstable ABL to develop over a period of 15 000 s, and the surface roughness and the surface heating rate were chosen so that the resulting ABL characteristics closely matched the values in Table I. Based on an analysis of available radiosonde data, a temperature inversion was also applied at $z = 1500$ m to limit the growth of the ABL in the vertical direction. After developing the precursor, an approximate 1000 s window was then selected for the turbine simulation to run.

The wind turbine simulations included a total of 558 turbines across five wind farms (King Plains, Armadillo Flats, Breckenridge, Chisholm View, and Thunder Ranch). The simulations used an actuator disk model to represent the turbine forces, and, for the 88 turbines at King Plains, the actuator disk model in AMR-Wind was coupled with OpenFAST. This coupling allows the simulation to more accurately capture the blade aerodynamics, control system behavior, and structural loading using OpenFAST’s engineering models. For the OpenFAST actuator disk model, the blade aerodynamics are computed

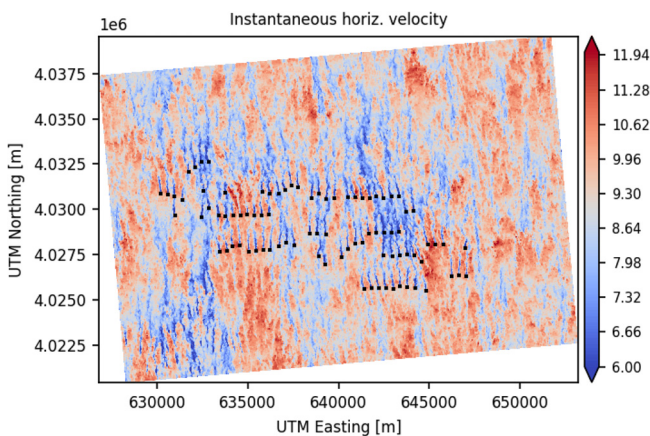


FIG. 2. Hub-height, instantaneous velocity contours of the wind farm simulation in an unstable ABL. The locations of all 88 King Plains wind turbines are indicated by the black markers.

using tabulated lift and drag polars, and the forces are then circumferentially averaged across the entire rotor disk. Rotor swirl effects are also retained, and play an important role in determining the structure of the downstream wakes (see Sec. II D). The turbine models used in this study were developed by scaling publicly available reference turbines to match the general characteristics of the actual turbines. The particular characteristics of the model used for the King Plains turbines are given in Table II and should provide a reasonable approximation of the GE 2.8-127 turbines at the site.

C. Convective structures and the classification of updraft/downdraft locations

The majority of the current study will focus on the analysis of wind turbine wakes from the King Plains wind farm site due to the concentration of instrumentation near that location. An instantaneous view of the hub-height wind field around King Plains is shown in Fig. 2, and the presence of large-scale convective structures similar to those in Fig. 1 can be easily seen. The size of the large-scale structures are typically several kilometers long and 1–2 km wide, which roughly matches the spacing and distribution of wind turbines within the wind farm itself.

The streaky nature of the convective structures is more evident in the time-averaged hub-height visualizations shown in Figs. 3 and 4 for the wind farm simulations and Fig. 5 for the equivalent precursor simulations. In both cases, the flow was averaged over an 11-min window after a 5-min transient period. This averaging window was chosen based on the length of simulation time available and alignment with the 10-min averaging windows used in many of the AWAKEN measurements. The averaged horizontal velocity images show the high-speed and low-speed streaks associated with the convective structures with deviations on the order of 1 m/s from the mean hub-height wind speed. The contours of the averaged hub-height vertical velocity also show noticeable streaks of upward and downward vertical motion of similar size to the convective structures themselves, and, for this simulation, the hub-height vertical velocity fluctuations were in the range $|W| < 0.5$ m/s.

The connection between the low-speed/high-speed streaks and updraft/downdraft motions, respectively, can be seen in the inflow velocity plane contours in Figs. 6 and 7. The inflow plane is located approximately 33 rotor diameters upstream of the first turbine row from King Plains (see Fig. 8) and is shown using averaged flow-field information from the precursor simulation to avoid possible wake contamination from upstream wind farms such as Armadillo Flats. In the wider view of the entire inflow plane shown in Fig. 6, the height of the

TABLE II. Characteristics of the OpenFAST wind turbine used for the turbines at King Plains. These parameters were created by scaling an IEA 3.4-130 reference turbine to match the general characteristics of the GE 2.8-127 turbine.

Parameter	Value
Rotor diameter	127 m
Hub height	90 m
Rated power	2.8 MW
Rated wind speed	10.7 m/s
Rated rotor speed	12.8 rpm

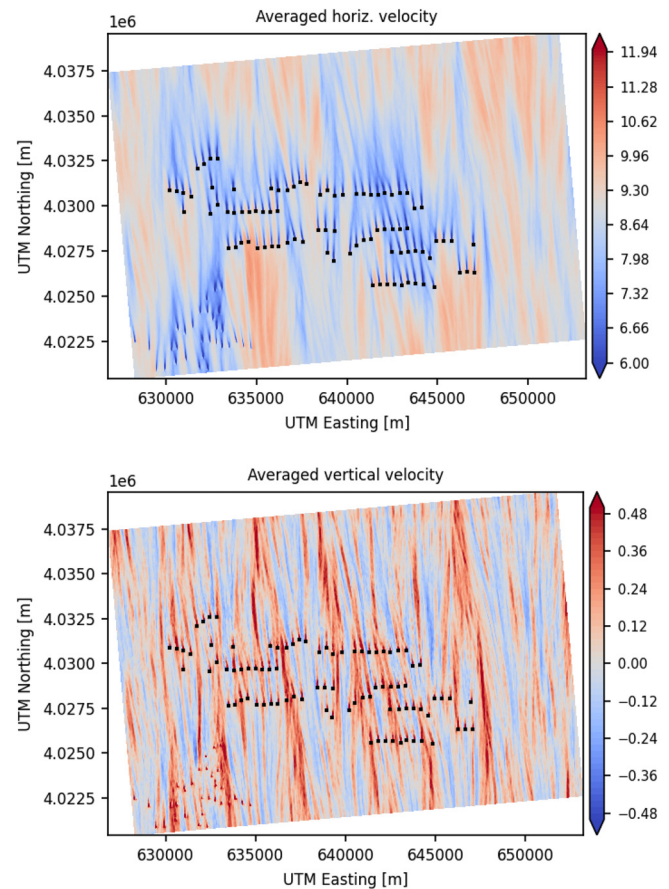


FIG. 3. Hub-height, time-averaged velocity contours of the wind farm simulation in an unstable ABL (top: averaged horizontal velocity, bottom: averaged vertical velocity). The locations of all 88 King Plains wind turbines are indicated by the black markers. Note the presence of wakes from the Armadillo Flats turbines in the southwest corner which are not included in this study.

convective structures is seen to persist past $z > 500$ m far above the upper rotor tips. A comparison of the vertical velocity and horizontal velocity contours also shows that updraft regions of the flows are associated with low-speed streaks in the flow while the downdraft regions are associated with the high-speed streaks.

The circulation patterns in the updraft and downdraft portions are shown more clearly in Fig. 7, which focuses on a smaller portion of the inflow plane. Here, the transition from the downward motion in one downdraft into an upward motion in an adjacent updraft is clearly visible using the directional arrows to represent the lateral velocity components. Figure 7 also shows the transport of higher velocity fluid toward the ground inside a downdraft, and, correspondingly, the upward motion of lower velocity fluid inside an updraft. This observation helps to explain the connection between updrafts and low-speed streaks and between downdrafts and high-speed streaks and is consistent with existing literature in turbulent boundary layers.³³

To quantify the impact of these convective structures on the turbine wakes, the King Plains turbines were categorized into updraft turbines and downdraft turbines based on their location relative to the

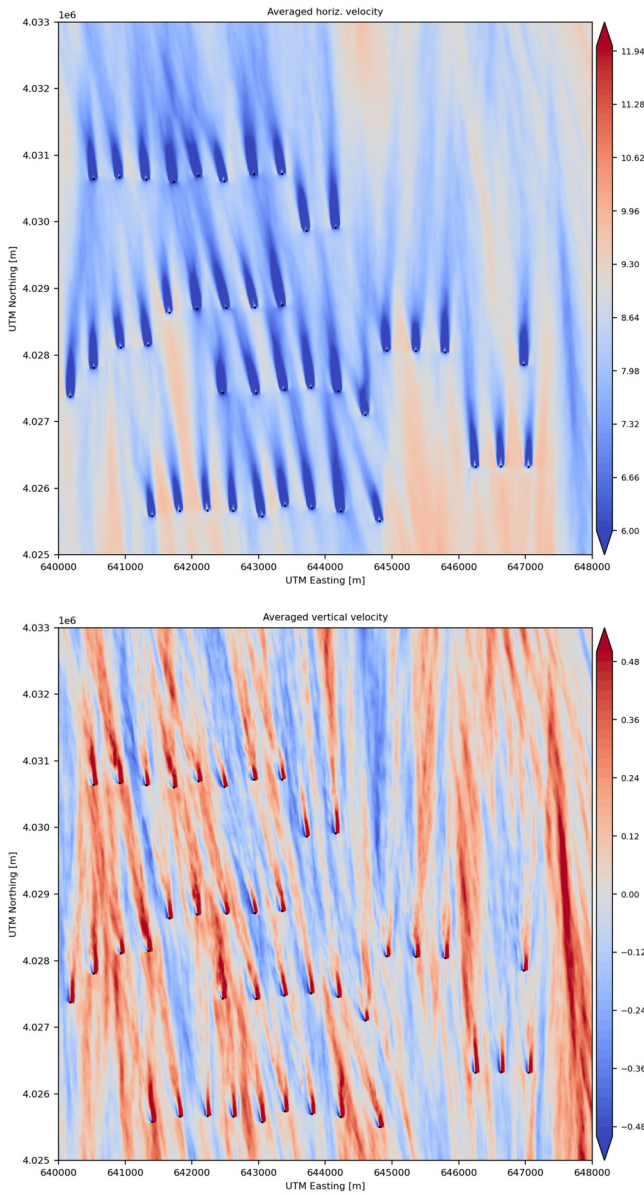


FIG. 4. Hub-height, time-averaged velocity contours of the same simulation as in Fig. 3, except showing only a close-up view of the Eastern section of the King Plains wind farm (top: averaged horizontal velocity, bottom: averaged vertical velocity).

structures and the locally observed flow. Of the 88 turbines at King Plains, the inflow wind speed for 27 turbines fell outside of the desired wind speed range ($9 \text{ m/s} \pm 10\%$) and were excluded from this categorization to control for turbine operation in the wake comparisons. This wind speed range was chosen based on observations of the averaged wake deficits (Fig. 12), which could be 20%–25% below the free stream values at 8D downstream. Restricting the inflow wind speed within the 10% limit excludes waked turbines, and the remaining turbines are separated by approximately 15–25D from their upstream neighbors.

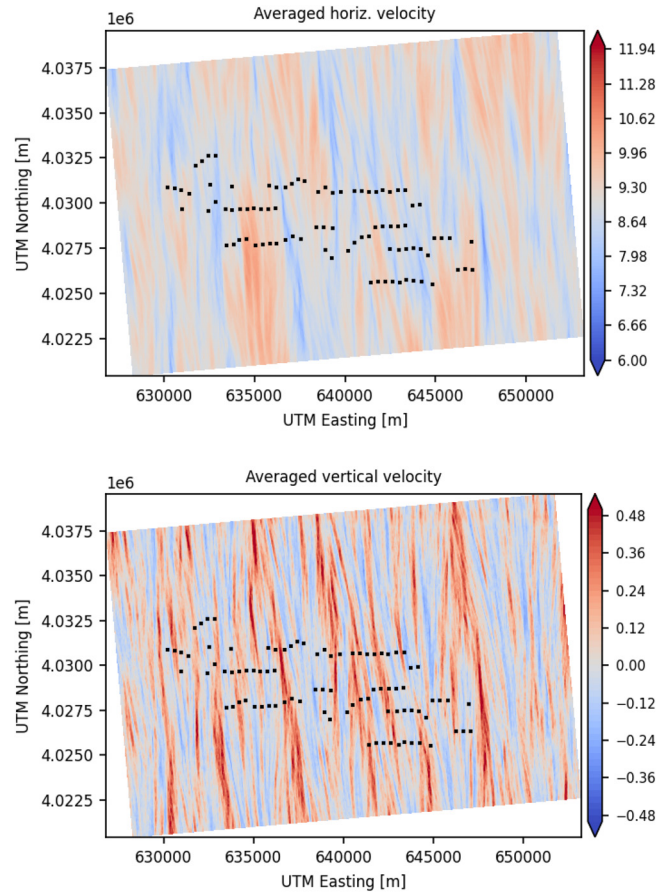


FIG. 5. Hub-height, time-averaged velocity contours of precursor unstable ABL without turbines (top: averaged horizontal velocity, bottom: averaged vertical velocity). The locations of all 88 King Plains wind turbines are indicated by the black markers (for reference only; they are not affecting the flow in this precursor simulation).

This process should allow the study to separate the effects of waking from the impacts of updrafts and downdrafts.

The remaining 61 turbines at King Plains were split into a group of 20 updraft turbines experiencing an average vertical velocity of 0.19 m/s and a group of 41 downdraft turbines with an averaged vertical velocity of -0.13 m/s . In general, the inflow wind speed for the updraft turbines was lower than the inflow wind speed for the downdraft turbines, which is consistent with the earlier connection between updrafts/downdrafts and low-speed/high-speed streaks. The difference in wind speed also led to an approximate 10% lower power output for the updraft turbines compared to the downdraft turbines.

In addition, a separate subset of turbines from the eastern portion of King Plains was categorized as “flat turbines.” The flat turbine group is comprised of 30 turbines whose wind speeds also fell within the desired wind speed range, but the collectively averaged vertical velocity was negligible. The averaged vertical velocity profile was $W(z) \approx 0.0 \text{ m/s}$, so this group is used to illustrate the behavior of turbine wakes in neither updrafts nor downdrafts. Details on the locations of the updraft, downdraft, and flat turbine groups are shown in Fig. 8 and Table III.

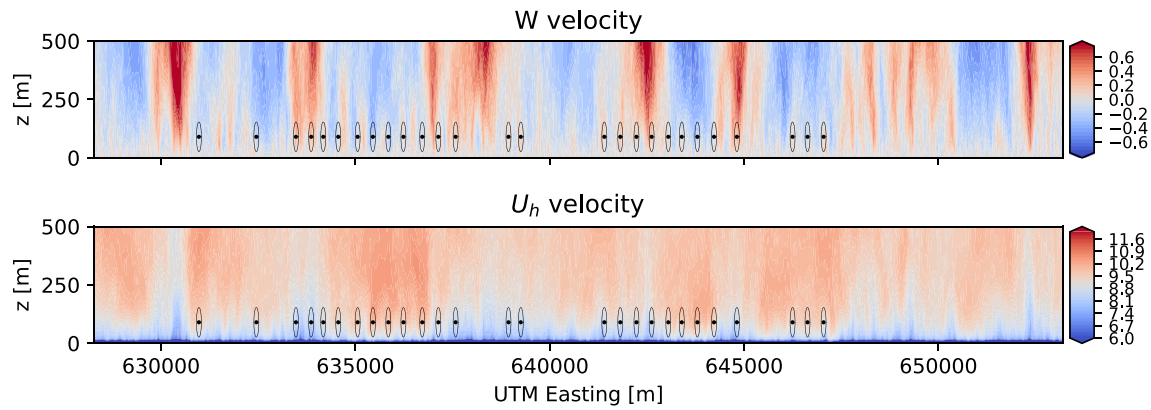


FIG. 6. Vertical and horizontal velocity contours on the upstream inflow plane to King Plains. The location of the inflow plane relative to wind farm turbines is shown in Fig. 8. (top: averaged vertical velocity; bottom: averaged horizontal velocity). The location and size of the first row of King Plains turbines are given by the rotor disk outlines.

Note that a similar classification analysis of the updraft and downdraft velocities as in Fig. 8 and Table III was performed from field data to assess the relevance of the up and downdrafts discussed herein to real wind farms. The measurement data were taken from a ground-based Halo XR scanning lidar (`sa1.lidar.z03.c1` on the Data Archive Portal³⁴) located at the Site A1. Site A1 is located approximately 300 m south of the first turbine row of the King Plains wind farm, and as such provides good characterization of the inflow to the wind farm for the predominant southerly winds. The vertical velocity reported by the scanning lidar was averaged between the range of 200–250 m above ground in an attempt to avoid influences of any turbine wakes for non-southerly wind directions. Analyzing over a year’s worth of measurements during the AWAKEN campaign and considering only unstable atmospheric stability as defined by Krishnamurthy *et al.*,²³ we calculated the number of instances of updrafts and downdrafts for a range of hub-height wind speeds approximately corresponding to the 9 m/s \pm 10% described by Table III. After adjusting for a positive mean bias of

approximately 0.05 m/s (i.e., $\sim 1^\circ$) in the vertical velocity data that agreed with the approximate slope of the terrain at this location, the threshold for up and downdrafts was set at ± 0.1 m/s to conservatively agree with the up and downdraft classifications of Table III. Using these definitions, updrafts were found to occur 20% of time while downdrafts occurred 44% of the time. Granted that the vertical velocity magnitudes considered here are not far from the limit of the lidar’s resolution, these numbers do suggest that the up and downdrafts as defined herein occur a significant percent of the time at the King Plains wind farm. It is also noted that the ratio of downdrafts to updrafts at roughly 2:1 matches between the measurement and the LES simulation, though the significance of this match is not certain.

D. Impact of convective structures on turbine wakes

Once the turbines in the King Plains wind farm have been classified into updraft and downdraft categories using the definitions in Sec. II C,

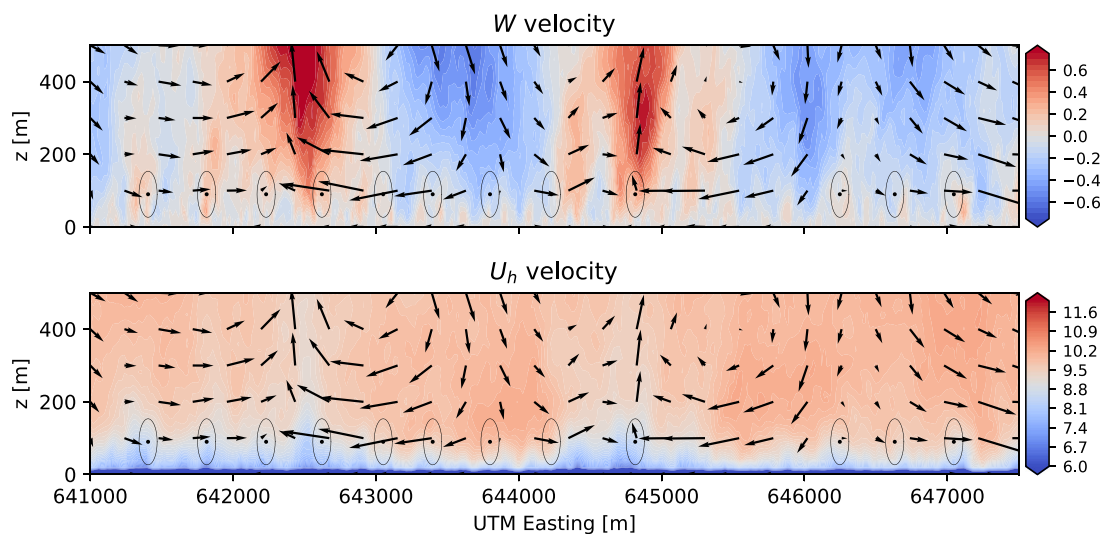


FIG. 7. A close-in view of the same velocity contours shown in Fig. 6 (top: averaged vertical velocity; bottom: averaged horizontal velocity), with the overlaid arrows depicting the lateral and vertical velocities on the plane. The location and size of the first row of King Plains turbines are given by the rotor disk outlines.

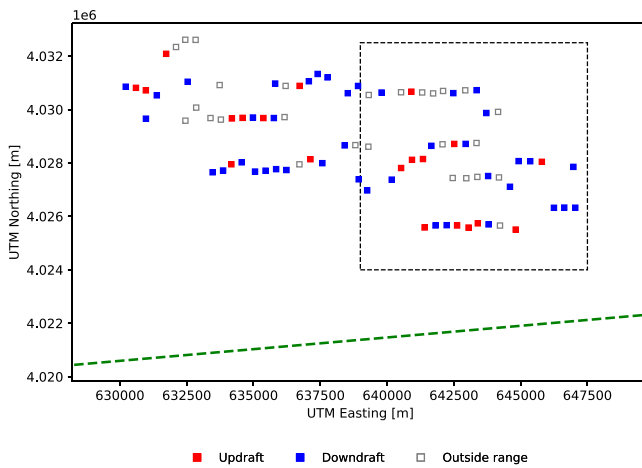


FIG. 8. Classification of King Plains turbines. The updraft and downdraft turbines inside the dashed rectangle collectively experience negligible vertical velocity. The dashed green line indicates the location of the inflow plane plotted in Figs. 6 and 7.

the impact of the convective structures on turbine wake evolution can be evaluated. First, it is important to note that the actuator disk turbine models used in the simulations includes circulation and the effect of swirl in the wake. This leads to a naturally occurring upward and downward region of the wake immediately downstream of every turbine. The vertical velocity contours shown in Fig. 9, averaged across all turbines in the downdraft, flat, and updraft categories, show that the large-scale structures can amplify or suppress the upward or downward swirl effects depending on whether they are in the updraft or downdraft regions, respectively. Note the model of the GE 2.8-127 used in this simulation also includes a small amount of shaft tilt ($\sim 5^\circ$), which increases the bias toward upward swirl effects.

A similar qualitative view of the difference can be seen in the rotor plane velocity and turbulent kinetic energy (TKE) contour plots in Figs. 10 and 11, respectively. These figures show the time-averaged and ensemble-averaged velocity and TKE across all turbines in the downdraft and updraft categories. The difference in wake shape is particularly apparent in the contours of the normalized horizontal velocity, $U_h/U_{h,precursor}$. At the turbine location, $x/D = 0$, the wake edge directly aligns with the rotor disk edge. For the downstream locations, the wakes in the downdraft locations are flattened while wakes in the updraft locations are vertically stretched above the upper rotor tip. In the far-wake region, past ($x/D \geq 8$), the wakes in the updraft locations also mix faster than the downdraft locations and consequently have faster wake recovery.

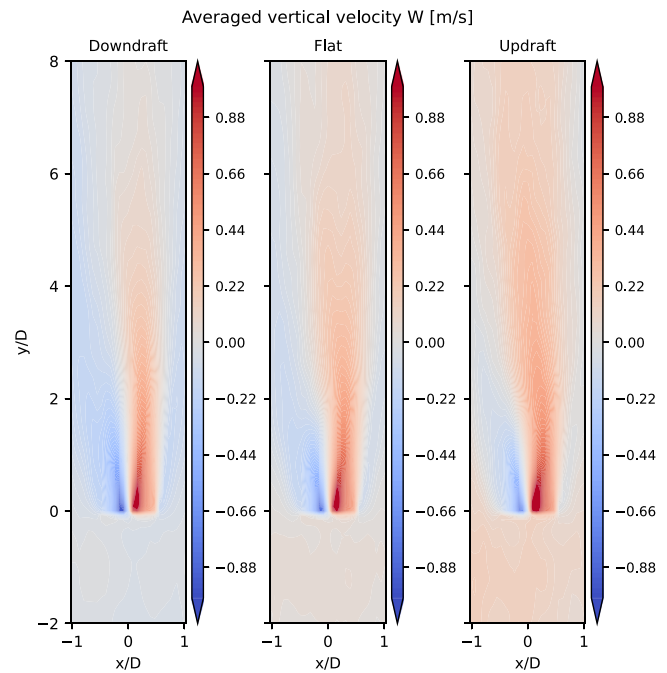


FIG. 9. Averaged vertical velocity W on the hub-height plane for all turbines in the downdraft, flat, and updraft regions of the flow. The view of the turbines is top-down, viewing of the wakes from above looking downward, with the inflow wind coming from the bottom.

The distribution of TKE on the rotor planes in Fig. 11 also shows differences between the wakes in the updraft and downdraft locations. Immediately downstream of the turbine locations, we see that there is a stronger TKE distribution for the wakes in the updraft locations. The updraft flow in the convective structures also transports the TKE to higher altitudes in the ABL compared to the wakes for the downdraft turbines.

A more quantitative comparison of the wake evolution is available in the comparisons of the velocity profiles at different distances upstream and downstream of the turbine. In Fig. 12, profiles of the normalized horizontal velocity, $U_h/U_{h,precursor}$, show a similar phenomenon as the earlier rotor plane contours. In the near-wake region, $x/D \leq 2$, there is a larger wake deficit for the updraft cases due to the slightly lower inflow velocity and higher thrust coefficients for the updraft turbines. However, for the downstream locations, $x/D \geq 4$, the faster wake recovery for the updraft turbines is apparent, and the greater penetration of the wake into the ABL can also be seen.

TABLE III. Classification of the King Plains turbines that fall within the wind speed range of $9 \text{ m/s} \pm 10\%$. The locations of the turbines are shown in Fig. 8.

Group	Number of wind turbines	Averaged hub-height wind speed (m/s)	Averaged vertical velocity (m/s)	Averaged power per turbine (kW)
Turbines in WS range	61	8.83	-0.0242	
Updraft turbines	20	8.57	0.1878	1890.6
Downdraft turbines	41	8.96	-0.1276	2096.8
Flat turbines	30	8.41	0.0028	1832.0

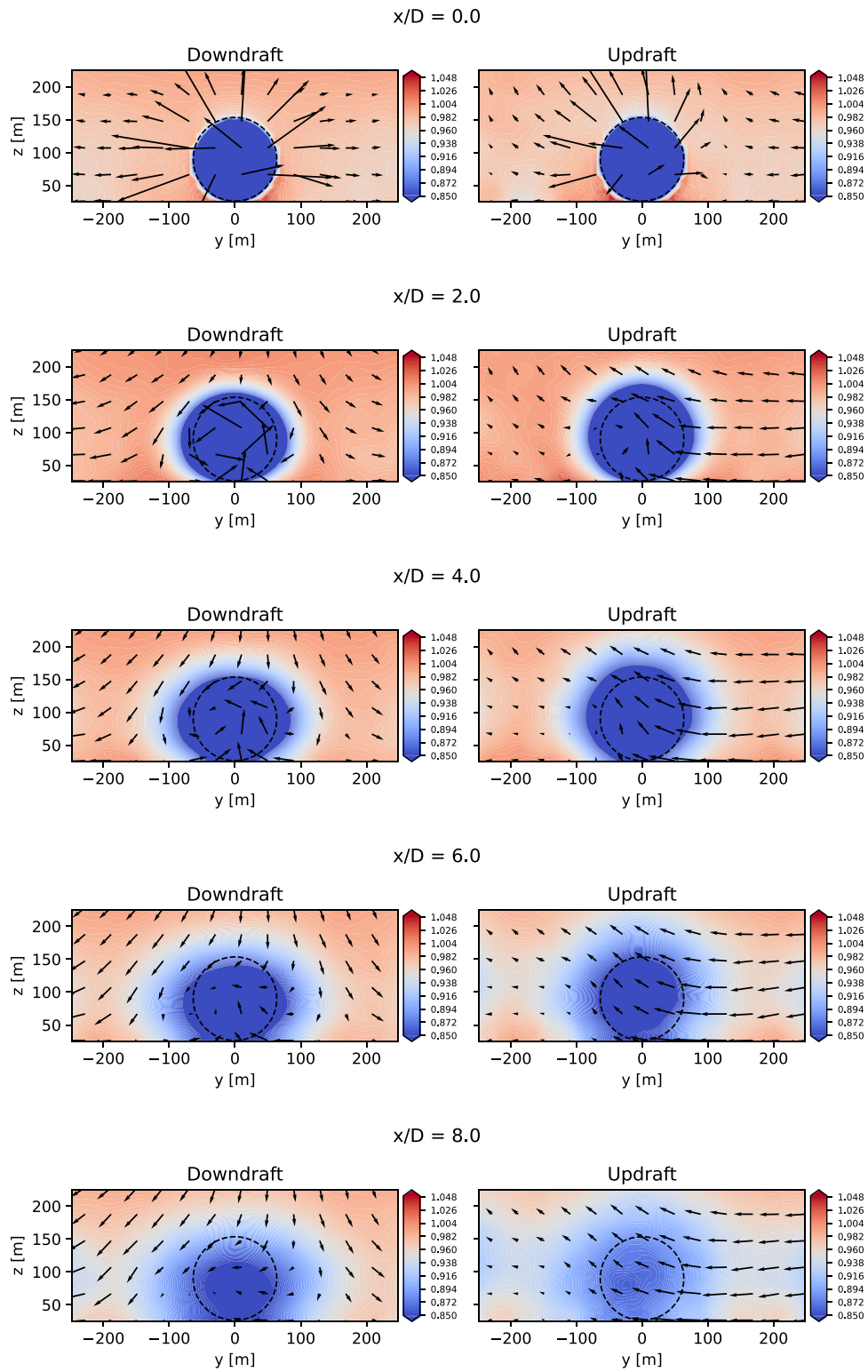


FIG. 10. Time-averaged contours of the normalized streamwise velocity, $U_h/U_{h,precursor}$, on the downstream rotor planes for the updraft (right column) and downdraft (left column) turbines at $x/D=0, 2, 4, 6,$ and 8 downstream. The overlaid arrows show the lateral and vertical velocities at each downstream location.

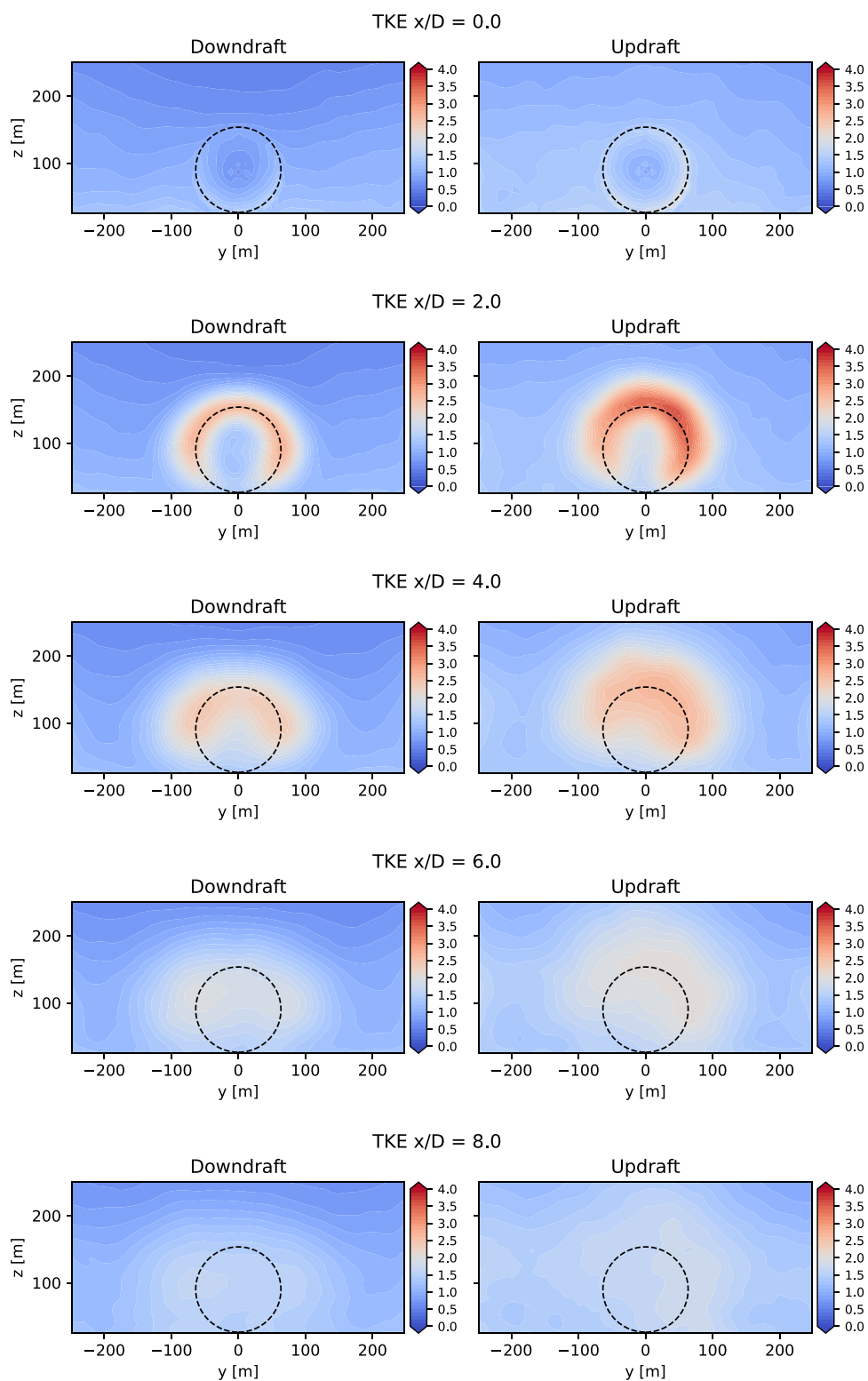


FIG. 11. Time-averaged contours of the TKE on the downstream rotor planes for the updraft (right column) and downdraft (left column) turbines at $x/D = 0, 2, 4, 6,$ and 8 downstream.

02 December 2024 22:33:56

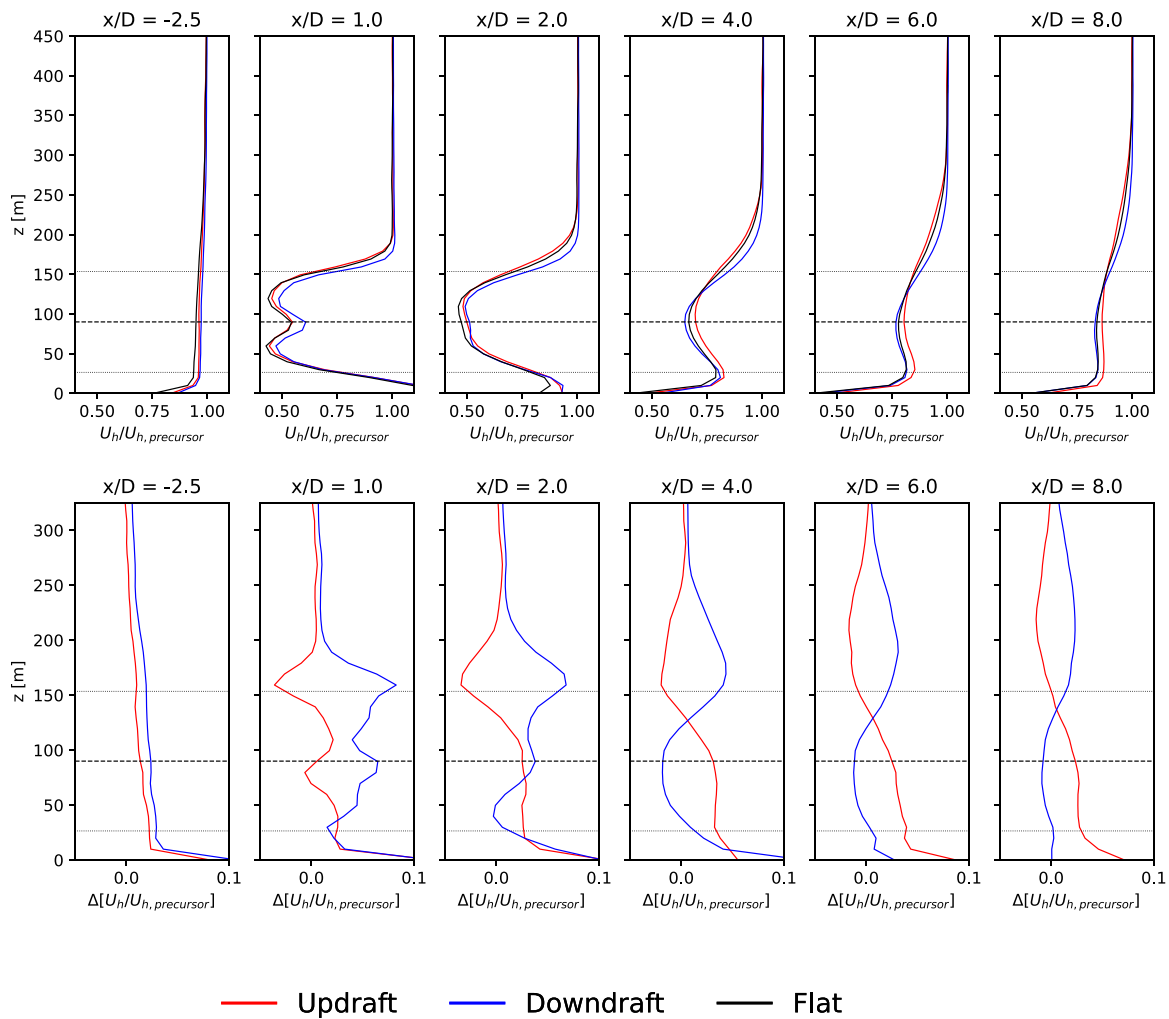


FIG. 12. Top: time-averaged, normalized streamwise velocity, $U_h/U_{h,precursor}$, profiles for turbine wakes in updraft (red), downdraft (blue), and flat (black) regions of large-scale convective structures. The horizontal lines correspond to the turbine hub height and upper/lower rotor tips. Bottom: The difference in $U_h/U_{h,precursor}$ between the updraft and flat profiles (red), and between the downdraft and flat profiles (blue).

In Fig. 13, the vertical velocities for the updraft, downdraft, and flat turbine categories are shown as well as the profiles for the wind farm and precursor runs for comparison. Immediately upstream of the turbine and in the near-wake region, up to $x/D = 2.0$, the presence of the operating turbines enhances the vertical velocity in both the updraft and downdraft cases. This additional vertical velocity is due to the blockage effect, where the incoming flow is decelerated and deflected upward around the wind turbines. This deflection results in the difference between the vertical velocity profiles of the wind farm runs and precursor runs in Fig. 13.

A comparison of the TKE profiles in Fig. 14 provides additional context to the earlier observations from the rotor plane comparisons. The higher vertical velocity observed in the updraft flows transports additional TKE to higher elevations. This is seen in the upstream profiles at $x/D = -2.5$, where the downdraft turbines experience less turbulent inflow compared to the updraft turbines. In the near wake, the

largest TKE values are seen near the upper rotor tips of the updraft turbines. The positive vertical velocity also redistributes the wake-generated turbulence: for $x/D \geq 4.0$, larger TKE values can be seen at elevations of $z > 250$ m.

The transport of horizontal momentum in the vertical direction in this simulation can also be illustrated through the time-averaged Reynolds stress, $\langle v'w' \rangle$ in Fig. 15. Here, the v' velocities fluctuations denote the streamwise velocity fluctuations in the domain as the flow is primarily aligned with the positive y axis. The most negative values of $\langle v'w' \rangle$ are seen for the updraft turbine cases, which corresponds to the transport of lower-speed-velocity fluctuations upward. While the vertical velocities in the wind farm simulation quickly revert to the precursor values above the rotor disk for $x/D \geq 4.0$, the excess $\langle v'w' \rangle$ Reynolds transport persist at high elevations up to $x/D = 8.0$.

Finally, the effect of the convective structures on the temperature profiles in the turbine wakes can be seen in Fig. 16. In general, the

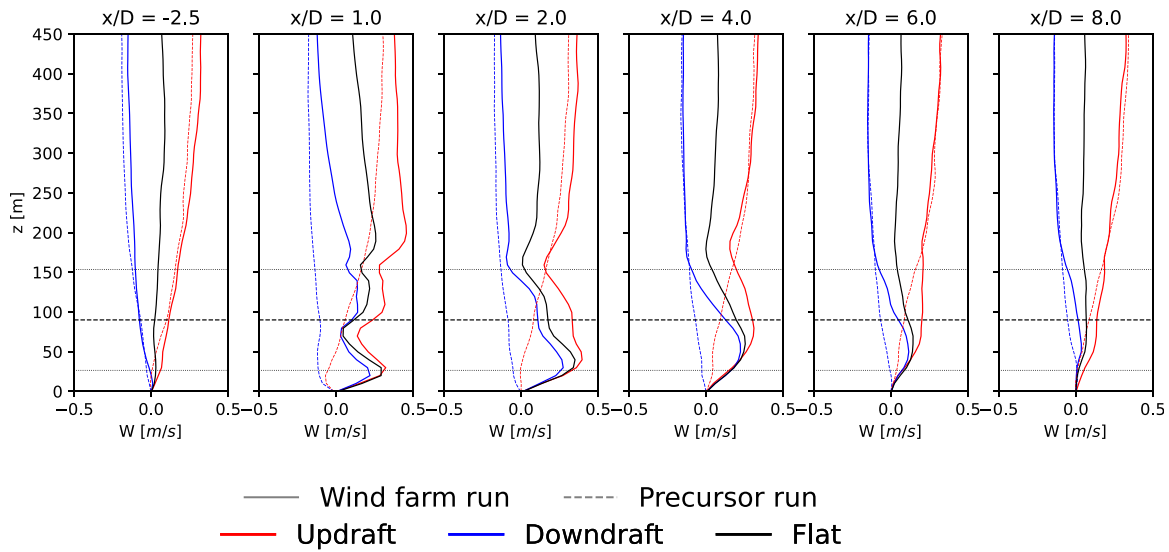


FIG. 13. Time-averaged vertical velocity profiles for turbine wakes in updraft (red), downdraft (blue), and flat (black) regions. Both the wind farm simulation (solid lines) and precursor simulation (dashed lines) profiles are shown. The horizontal lines correspond to the turbine hub height and upper/lower rotor tips.

temperature field in the updraft and downdraft regions follows the upstream behavior of both the velocity and the TKE fields. In regions of positive vertical velocity, higher temperature flow is transported upward, and lower temperature flow is brought downward in regions of negative vertical velocity, although the difference is relatively minor. These profiles also show that mixing of the temperature field due to the turbine wake is negligible in this simulation, and there is no substantive difference between the precursor temperature field and the wind farm case.

III. A SIMPLIFIED TWO-DIMENSIONAL MODEL

While the preceding discussion showed that LES can capture the complex interactions between the turbine wake field and the convective structures in the unstable ABL, it remains a computationally expensive approach to predict wake behavior. One major restriction on many current wake prediction methods such as the Jensen¹⁴ or Ainslie¹⁷ model is the assumption of steady inflow profiles with no vertical velocity and the absence of convective structures in the ABL.

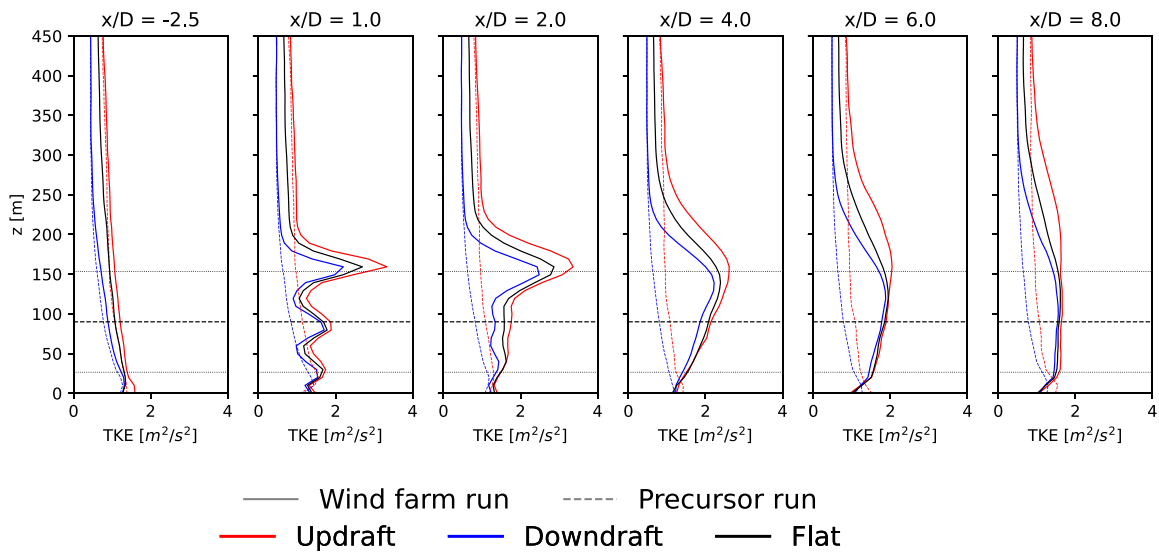


FIG. 14. Time-averaged profiles of TKE for turbine wakes in updraft (red), downdraft (blue), and flat (black) regions. Both the wind farm simulation (solid lines) and precursor simulation (dashed lines) profiles are shown. The horizontal lines correspond to the turbine hub-height and upper/lower rotor tips.

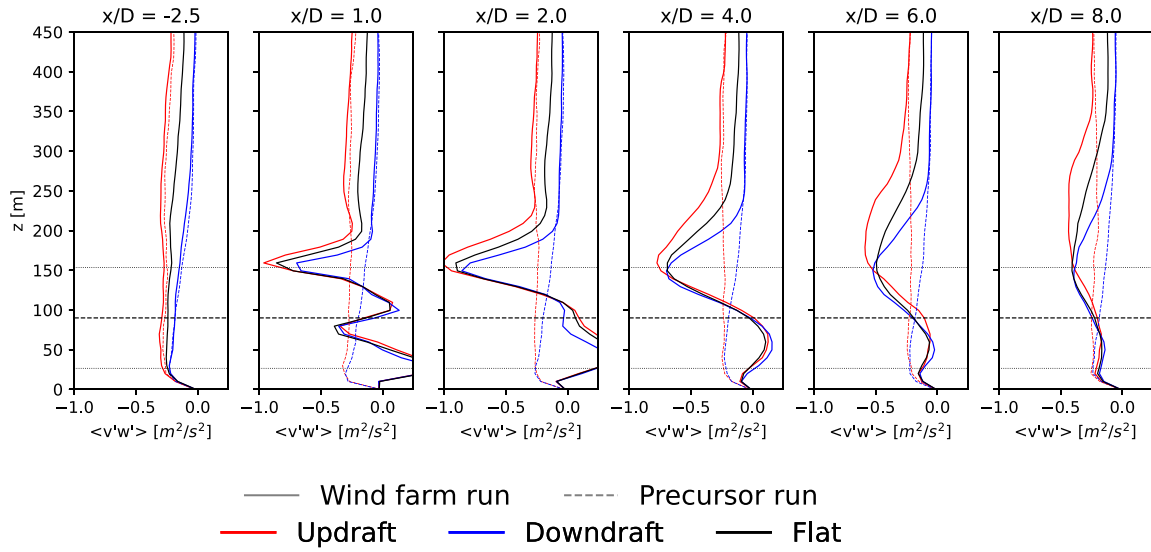


FIG. 15. Time-averaged profiles of the Reynolds stress $\langle v'w' \rangle$ term showing the vertical transport of the streamwise velocity fluctuations v' . Both the wind farm simulation (solid lines) and precursor simulation (dashed lines) profiles are shown. The horizontal lines correspond to the turbine hub height and upper/lower rotor tips.

In this section, a simplified model of the wake behavior is derived from a 2D RANS formulation. The 2D model considers the downstream (x) evolution of wake profiles in the vertical (z) direction, and neglects variations in the lateral (y) direction. This simple, efficient model retains the vertical velocity terms and also includes the atmospheric stratification effects. However, the 2D nature of the model excludes the possibility of capturing the 3D nature of the convective rolls or the swirling nature of the turbine wake. Therefore, the primary goal of the simplified model is not to facilitate a direct quantitative comparison to the LES results, but to focus on capturing the essential vertical modifications of wake properties and to provide a basis for future modeling efforts.

A. Mathematical formulation

The simplified model is based on the RANS equations using a standard k - ϵ closure model with a Boussinesq buoyancy approximation. Alinot and Masson³⁵ used these equations to predict the behavior of ABLs in different conditions of thermal stratification, and their model serves as a starting point for the RANS formulation here. To avoid solving the full elliptic problem, we apply the boundary layer approximation to the RANS equations, meaning that second-order derivatives in x are small relative to other terms in the formulation, the spanwise or lateral derivatives in y can be neglected, and the vertical pressure gradient is decoupled from velocity. This leads to a 2D parabolic system that can be marched in the downstream direction. However, because the topology of the model problem has also changed, the wake expansion and recovery in the simplified formulation may not match results from the full 3D LES. Nevertheless, the impact of the updraft and downdraft flows can still be illustrated through this simplified approach.

The resulting equations are:

$$u \frac{\partial u}{\partial x} + w \frac{\partial u}{\partial z} = -\frac{1}{\rho} \frac{\partial p}{\partial x} + \frac{\partial}{\partial z} \left((\nu + \nu_t) \frac{\partial u}{\partial z} \right), \quad (1a)$$

$$\frac{1}{\rho} \frac{\partial p}{\partial z} = g\beta(T - T_0), \quad (1b)$$

$$\frac{\partial u}{\partial x} + \frac{\partial w}{\partial z} = 0, \quad (1c)$$

$$u \frac{\partial k}{\partial x} + w \frac{\partial k}{\partial z} = \nu_t \left(\frac{\partial u}{\partial z} \right)^2 - \epsilon + \frac{\partial}{\partial z} \left(\left(\nu + \frac{\nu_t}{\sigma_k} \right) \frac{\partial k}{\partial z} \right) + G_B, \quad (1d)$$

$$u \frac{\partial \epsilon}{\partial x} + w \frac{\partial \epsilon}{\partial z} = \frac{C_{1\epsilon}}{\mathcal{T}} \left[\nu_t \left(\frac{\partial u}{\partial z} \right)^2 + (1 - C_{3\epsilon}) G_B \right] - \frac{C_{2\epsilon}}{\mathcal{T}} \epsilon + \frac{\partial}{\partial z} \left(\left(\nu + \frac{\nu_t}{\sigma_\epsilon} \right) \frac{\partial \epsilon}{\partial z} \right), \quad (1e)$$

$$u \frac{\partial T}{\partial x} + w \frac{\partial T}{\partial z} = \frac{\nu}{Pr} \frac{\partial^2 T}{\partial z^2}, \quad (1f)$$

where u and w are the streamwise and vertical velocity components, k and ϵ are the turbulent kinetic energy and dissipation, and T is the temperature. The eddy-viscosity model $\nu_t = C_\mu k \mathcal{T}$ is specified by the timescale $\mathcal{T} = \max\{\frac{k}{\epsilon}, 6\sqrt{\frac{\nu}{\epsilon}}\}$, which ensures that the turbulent timescale does not go below the Kolmogorov timescale near the ground.³⁶ G_B represents the production (or destruction) of turbulent kinetic energy by buoyancy forces and is given by:

$$G_B = \beta g \frac{\nu_t}{Pr} \left(\frac{\partial T}{\partial z} - \frac{g}{c_p} \right). \quad (2)$$

The following constants for the k - ϵ model are used:

$$C_{1\epsilon} = 1.76, \quad C_{2\epsilon} = 1.92, \quad C_{3\epsilon} = 0.033, \\ C_\mu = 5.82^{-2}, \quad \sigma_k = 1.0, \quad \sigma_\epsilon = 1.3,$$

which are based on the values proposed by Alinot and Masson³⁵ for ABLs. It is important to acknowledge that, in the derivation of these constants, Alinot and Masson³⁵ demonstrated that the standard k - ϵ

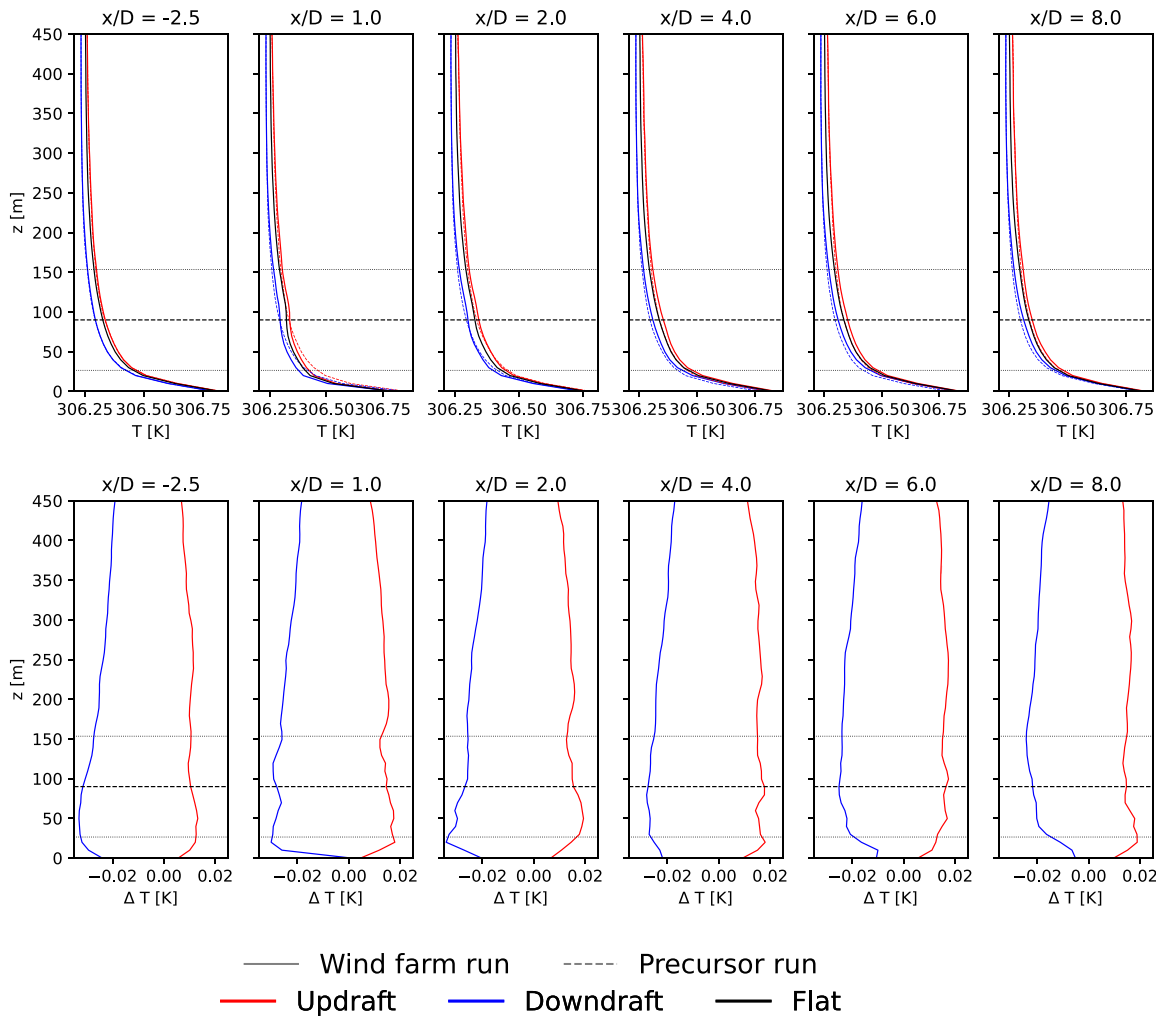


FIG. 16. Top: time-averaged temperature profiles for turbine wakes in updraft (red), downdraft (blue), and flat (black) regions. Both the wind farm simulation (solid lines) and precursor simulation (dashed lines) profiles are shown. The horizontal lines correspond to the turbine hub height and upper/lower rotor tips. Bottom: the difference in temperature between the updraft and flat temperature profiles (red), and the difference between the downdraft and flat temperature profiles (blue).

constants proposed by Jones and Launder³⁷ needed to be adjusted for ABL flows. Therefore, these constants may need further modifications for wakes situated in an ABL, which will be explored as part of future model developments. Additionally, the standard values are used for density, $\rho = 1.225 \text{ kg/m}^3$, kinematic viscosity, $\nu = 1.47 \times 10^{-5} \text{ m}^2/\text{s}$, specific heat, $c_p = 1006.43 \text{ J/kg}$, thermal expansion coefficient, $\beta = 0.0033/\text{K}$, Prandtl number, $Pr = 0.7$, and gravitational constant, $g = -9.8 \text{ m/s}^2$.

B. Numerical solution

Equations (1a)–(1f) are discretized on a uniform grid in the z -direction using a second-order centered difference method. The vertical domain ranges from $z_{\text{bot}} = 2.5$ to $z_{\text{top}} = 450 \text{ m}$ with a spacing of $\Delta z = 2.5 \text{ m}$. In the x -direction, the equations are discretized around the cell centers and a Crank–Nicolson method is used to march 7D

downstream of the initial condition at $x = x_0$ with uniform step sizes of $\Delta x = 10 \text{ m}$. An iterative solver is used to solve the resulting tridiagonal system advancing the solution from one x -location to the next.

Three different RANS simulations are performed representing an updraft, downdraft, and flat scenario. Since updrafts and downdrafts cannot be physically generated by the 2D RANS model, these conditions are imposed on the flow through the initial and boundary values of the w -velocity. The initial conditions for w are taken to be linear profiles that extend from 0 at the ground to the boundary values $w_{\text{flat}}(z_{\text{top}}) = 0$, $w_{\text{updraft}}(z_{\text{top}}) = 0.3$, and $w_{\text{downdraft}}(z_{\text{top}}) = -0.3$. Further, the continuity relation (1c) only allows for one boundary condition to be imposed on w . To maintain differences in the vertical velocity profiles for the updraft, downdraft, and flat cases, the values for w at z_{top} are, therefore, fixed, which means a finite vertical velocity develops at the ground as the wake evolves. This is a limitation of the 2D model and its implications are discussed in Sec. IV.

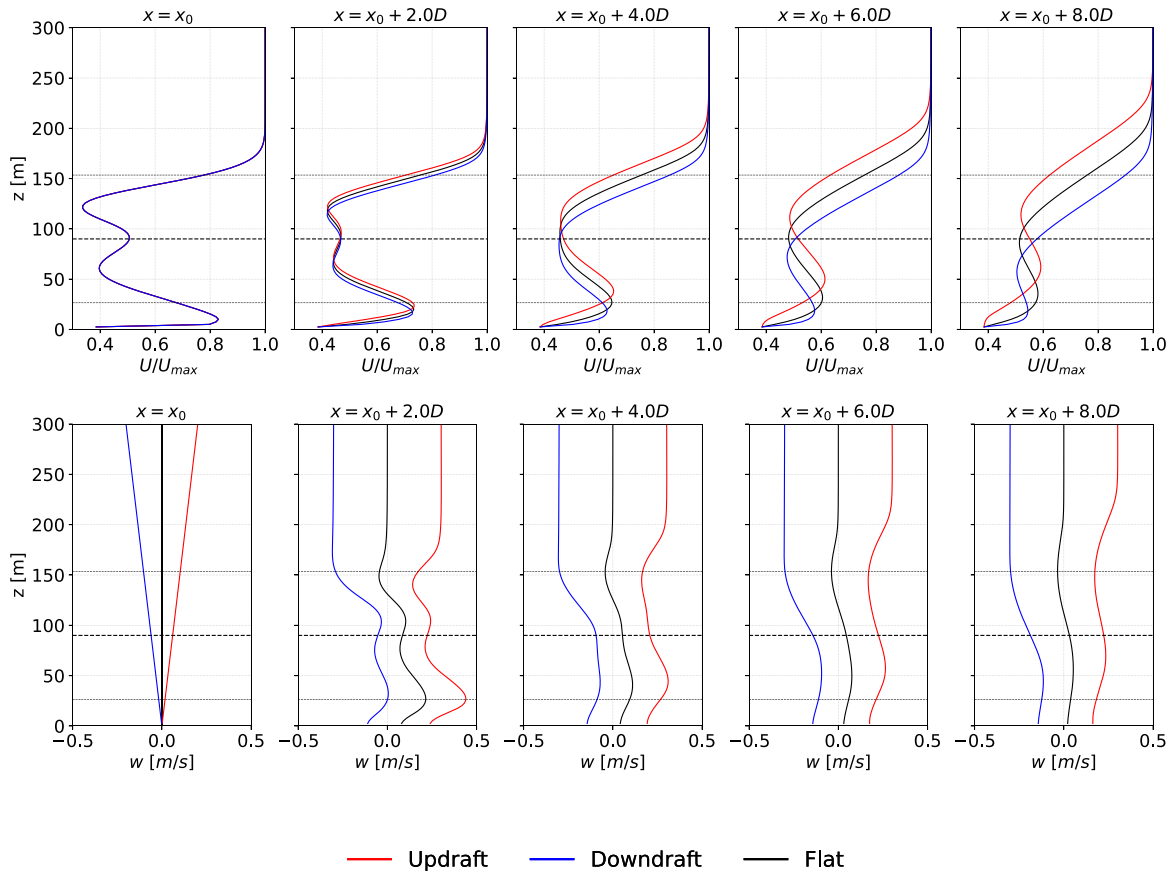


FIG. 17. Normalized RANS streamwise velocity, U/U_{max} , profiles (top) and vertical velocity, w , profiles (bottom) for turbine wakes in updraft, downdraft, and flat regions.

In each case, the initial u -velocity is modeled with a combination of three Gaussian profiles,

$$u(x_0, z) = A_1 e^{-(z-z_1)^2/2\sigma_1^2} + A_2 e^{-(z-z_2)^2/2\sigma_2^2} + A_3 e^{-(z-z_3)^2/2\sigma_3^2} + C, \quad (3)$$

with constants chosen to roughly match the curvature in the LES profiles 1D downstream of the turbine ($A_1 = -6.0$, $\sigma_1 = 30.0$, $z_1 = 60.0$, $A_2 = -6.0$, $\sigma_2 = 20.0$, $z_2 = 125.0$, $A_3 = -1.5$, $\sigma_3 = 5.0$, $z_3 = 0.0$, and $C = 10$). Using the same initial conditions for all three cases eliminates differences in the wake due to higher or lower wind speed from the inflow conditions. The initial profile for k is based on the square of the velocity gradient, $k \sim (\partial u / \partial z)^2$, such that $\sqrt{3 \max(k)} / 2 = 0.1$, and the initial ε is taken to balance turbulent kinetic energy production, i.e., $\varepsilon = \sqrt{C_{1\varepsilon} k^2 (\partial u / \partial z)^2}$. Finally, an initial linear temperature profile is imposed with slope $\partial T / \partial z = -0.0011$ K/m to include unstable buoyancy effects on the wake. The magnitude of the temperature gradient is greater than that of the dry adiabatic lapse rate, g/c_p , so that G_B is positive, leading to an increase in k production and dissipation consistent with unstable stratification. Note that a small streamwise pressure gradient arises due to temperature changes in x , which can be obtained by integrating (1b) in z and differentiating in x so that,

$$\frac{\partial p}{\partial x} = \int_0^z \rho g \beta \frac{\partial T}{\partial x} dz. \quad (4)$$

The following boundary conditions are applied at z_{bot} and z_{top} :

$$\begin{aligned} u(z_{bot}) &= \frac{u_*}{C_K} \ln\left(\frac{z}{z_0}\right), & \frac{\partial u}{\partial z}(z_{top}) &= 0, \\ k(z_{bot}) &= 5.48 u_*^2, & \frac{\partial k}{\partial z}(z_{top}) &= 0, \\ \varepsilon(z_{bot}) &= \frac{u_*^3}{C_K z_{bot}}, & \frac{\partial \varepsilon}{\partial z}(z_{top}) &= 0, \\ \frac{\partial T}{\partial z}(z_{bot}) &= -0.0011, & \frac{\partial T}{\partial z}(z_{top}) &= -0.0011, \end{aligned}$$

where the values for u , k , and ε are based on Monin–Obukhov similarity theory for ABL flows over a flat terrain in neutral conditions.³⁵ The friction velocity, $u_* = 0.575652$, and surface roughness, $z_0 = 0.15$, are taken to match the values from the unstable ABL LES precursor and $C_K = 0.42$ is the von Kármán constant.

C. Model results

The evolution of the simplified wake by the RANS model is shown in Figs. 17–19 for the updraft, downdraft, and flat scenarios.

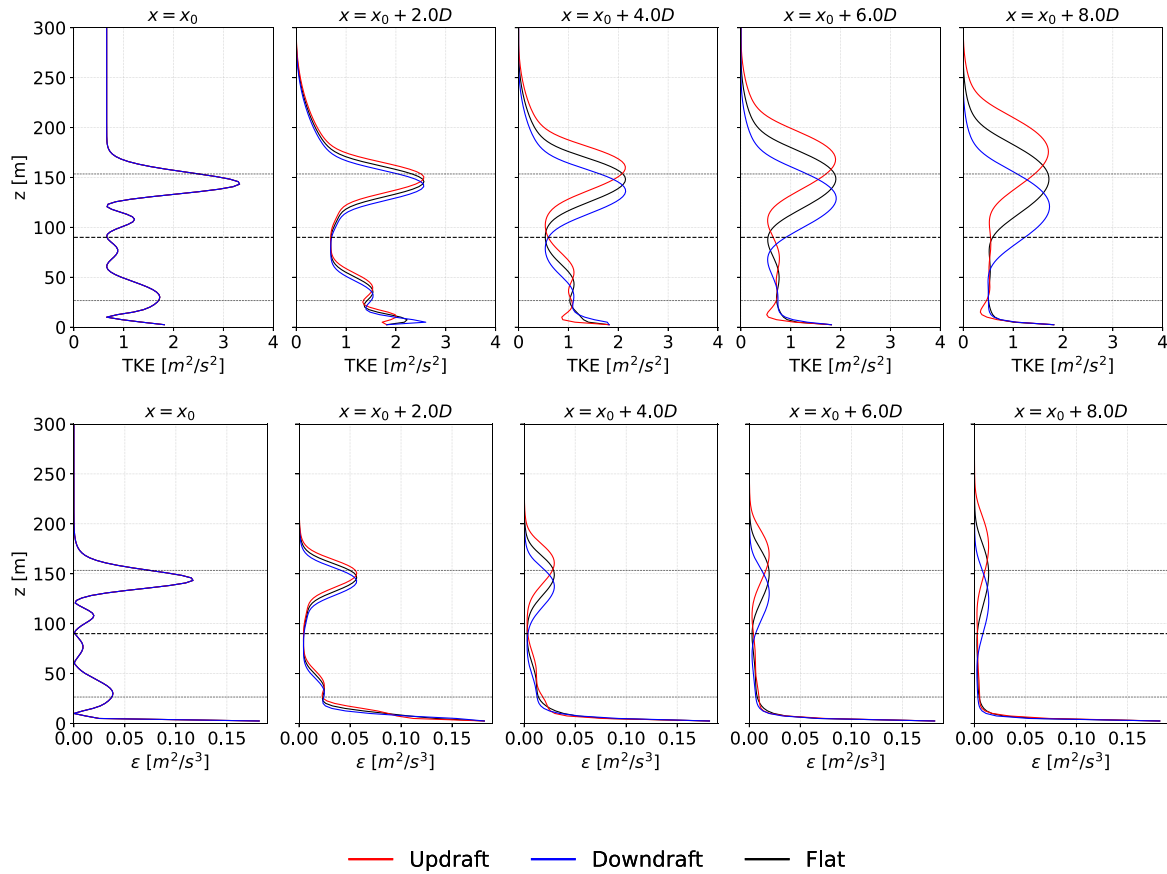


FIG. 18. Evolution of the RANS TKE (top) and ϵ (bottom) profiles for turbine wakes in updraft, downdraft, and flat regions.

Recall that the objective is to assess whether the RANS model can qualitatively capture the effects of updrafts and downdrafts on the evolution of the modeled wake, as well as to explore the applicability and limitations of a 2D model in this context. For the wakes experiencing a

local updraft, the lower momentum flow from the wake is transported upward past the rotor upper tips, and higher momentum fluid is lifted up into the rotor disk region (see Fig. 17). Conversely, for wakes in the downdraft flow regions, the vertical growth of the wake is depressed.

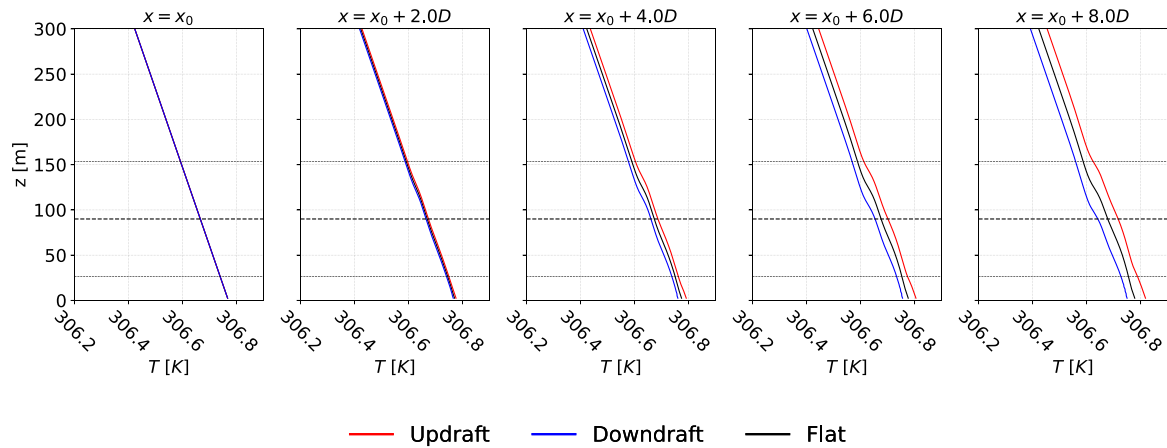


FIG. 19. Evolution of the RANS temperature profiles for turbine wakes in updraft, downdraft, and flat regions.

This behavior is similar to that observed in the streamwise velocity LES profiles shown in Fig. 12 and the rotor plane contours shown in Fig. 10. However, nonphysical vertical advection of momentum below the bottom rotor-tip is observed because of the finite vertical velocity near the ground, which is a clear defect of the 2D modeling assumptions and a deviation from the LES behavior in Fig. 12. The model also fails to represent the wake spreading in x far downstream (see Fig. 17). This may also be a fundamental limitation of 2D models because entraining momentum is considerably more challenging in 2D than in 3D, which delays wake recovery.

The behavior of the vertical velocity, w , also displays some similar characteristics to the LES predictions shown in Fig. 13. Inside the near-wake region, there is additional vertical velocity created due to the turbine wake itself causing a rightward shift in the w profiles for all cases. There is also an obvious departure from the LES solution near the ground, which is again due to the finite vertical velocity at z_{bot} resulting from the singular boundary condition imposed on the w -solution at z_{top} .

The RANS evolution of the modeled TKE distribution provides insights into the behavior of the TKE in the LES. As shown in Fig. 18, greater turbulence is transported into the ABL in the updraft case compared to the downdraft case, but the peak TKE values remain relatively unchanged. This suggests that the upward flow due to the convective structure does not increase production of TKE inside the wake itself but it can redistribute the turbulence so that some turbines experience higher TKE at the inflow, as seen in Fig. 14. Similarly, the greater transport of turbulence into the ABL by updrafts is accompanied by increased turbulent dissipation in the ABL, although the RANS results suggest dissipation diffuses more rapidly than TKE (see Fig. 18).

The simplified RANS model also predicts relatively minor changes to the evolution of the linear temperature profile in Fig. 19. As with the LES temperature profiles in Fig. 16, the updraft case shows a slight increase in the temperature in the domain, while the downdraft case has a slight temperature decrease.

Despite the ability of the RANS model to capture important wake modifications in the presence of updrafts and downdrafts, there are clear deficiencies in the model highlighted above that indicate further model developments are required. One avenue is to adjust the k - ϵ model constants, or to explore other RANS closure models beyond the k - ϵ model.^{13,36,38–41} However, several of the model deficiencies suggest a 2D formulation may be insufficient for fully capturing updraft/downdraft effects and that a 3D formulation is needed instead. This is reasonable since the 2D flow is nonvarying in the y -direction, preventing mixing of high or low-speed flow from the lateral sides. Ideally, the same principles developed here could be used to develop a parabolic 3D RANS formulation to march 2D wake cross sections downstream. With a 3D formulation, the circulation patterns corresponding to the large-scale structures could be superimposed on the mean inflow profiles, and the turbine wake swirl could also be included, providing a more complete picture of wake evolution. However, it is important to note that a 3D formulation would be more computationally expensive than the 2D formulation, so the current approach is still regarded as an efficient means of modeling general updrafts and downdrafts effects on the wake.

IV. CONCLUSIONS

In this study, we explored the impact of large-scale convective structures in an unstable ABL on turbine wake evolution. Simulation

data from an LES of the AWAKEN wind farm site by Cheung *et al.*¹¹ was analyzed, and the turbines at the King Plains wind farm were classified based on their locations in updraft or downdraft regions of the flow. The turbines located in updraft portions of a convective structure experienced lower inflow velocity and generated less power, but their wakes experienced faster wake recovery and mixed farther upward into the ABL. Conversely, turbines located in the downdraft regions generated more power due to the higher inflow velocities, but also resulted in slower wake recovery and less mixing of the wake above the upper rotor tips.

A simplified model of this wake interaction was developed based on the 2D RANS equations. This formulation used a standard k - ϵ closure model based on the Alinot and Masson³⁵ ABL model including stratification effects and resulted in a parabolic system that could be efficiently marched to determine the wake evolution. The RANS wake profiles captured the qualitative characteristics of the LES simulations including the upward motion of the wakes and TKE in cases where updrafts were present, and a general vertical contraction of the wake in downdraft regions.

Future research work on this topic may explore the long-term evolution of the wakes as multiple large-scale convective structures pass through the wind farm as well as other unstable ABL conditions matching those measured in the AWAKEN campaign. The effect of terrain, particularly the impact of terrain-induced vertical velocity, is also an important topic, and may be investigated using tools such as the Weather Research and Forecasting (WRF) model. The initial 2D RANS model developed in this study can also be extended to a 3D model to fully capture the modified shape of the turbine wakes. A 3D version of the RANS model will also better capture the full circulation patterns corresponding to the large-scale structures, and better model the wake recovery due to the inclusion of spanwise derivatives which are neglected in the 2D version. Such a 3D model would require a suitable actuator disk representation for turbine, but is relatively straightforward to implement. The evolution and merging of multiple turbine wakes and TKE fields would be possible in such a 3D model, and predicting the impacts of large-scale updrafts and downdrafts on wind farm performance is an important practical consequence. In addition, the appropriate k - ϵ model constants for this application should be investigated along with other potential closure models.

ACKNOWLEDGMENTS

This research was supported by the Wind Energy Technologies Office of the U.S. Department of Energy Office of Energy Efficiency and Renewable Energy. Sandia National Laboratories is a multimission laboratory managed and operated by National Technology & Engineering Solutions of Sandia, LLC, a wholly owned subsidiary of Honeywell International Inc., for the U.S. Department of Energy's National Nuclear Security Administration under Contract No. DE-NA0003525. The views expressed in the article do not necessarily represent the views of the U.S. Department of Energy or the United States Government. This research used resources of the Oak Ridge Leadership Computing Facility, which is a DOE Office of Science User Facility supported under Contract No. DE-AC05-00OR22725, which was provided through the ASCR Leadership Computing Challenge (ALCC) program. This work was authored in part by the National Renewable Energy Laboratory, operated by Alliance for Sustainable

Energy, LLC, for the U.S. Department of Energy (DOE) under Contract No. DE-AC36-08GO28308. Funding was provided by the U.S. Department of Energy Office of Energy Efficiency and Renewable Energy Wind Energy Technologies Office. The employee owns all right, title and interest in and to the article and is solely responsible for its contents. The U.S. Government retains and the publisher, by accepting the article for publication, acknowledges that the U.S. Government retains a nonexclusive, paid-up, irrevocable, worldwide license to publish or reproduce the published form of this work, or allow others to do so, for U.S. Government purposes. The DOE will provide public access to these results of federally sponsored research in accordance with the DOE Public Access Plan <https://www.energy.gov/downloads/doe-public-access-plan>.

AUTHOR DECLARATIONS

Conflict of Interest

The authors have no conflicts to disclose.

Author Contributions

Lawrence Cheung: Conceptualization (lead); Investigation (equal); Methodology (equal); Writing – original draft (equal); Writing – review & editing (equal). **Gopal Yalla:** Conceptualization (equal); Investigation (equal); Methodology (equal); Writing – original draft (equal); Writing – review & editing (equal). **Kenneth Brown:** Conceptualization (equal); Investigation (equal); Methodology (equal); Writing – original draft (equal); Writing – review & editing (equal). **Nathaniel deVelder:** Conceptualization (equal); Investigation (equal); Methodology (equal); Writing – original draft (equal); Writing – review & editing (equal). **Alan Hsieh:** Conceptualization (equal); Investigation (equal); Methodology (equal); Writing – original draft (equal); Writing – review & editing (equal). **Thomas Herges:** Conceptualization (equal); Investigation (equal); Methodology (equal); Project administration (equal); Writing – original draft (equal); Writing – review & editing (equal). **Daniel Houck:** Conceptualization (equal); Investigation (equal); Methodology (equal); Writing – original draft (equal); Writing – review & editing (equal). **David Maniaci:** Conceptualization (equal); Investigation (equal); Methodology (equal); Writing – original draft (equal); Writing – review & editing (equal). **Philip Sakievich:** Conceptualization (equal); Investigation (equal); Methodology (equal); Writing – original draft (equal); Writing – review & editing (equal). **Aliza Abraham:** Investigation (equal); Methodology (equal); Writing – original draft (equal); Writing – review & editing (equal).

DATA AVAILABILITY

The data that support the findings of this study are available from the corresponding author upon reasonable request.

REFERENCES

- ¹A. K. M. F. Hussain, “Coherent structures—Reality and myth,” *Phys. Fluids* **26**, 2816–2850 (1983).
- ²D. Etling and R. A. Brown, “Roll vortices in the planetary boundary layer: A review,” *Boundary-Layer Meteorol.* **65**, 215–248 (1993).
- ³L. Alcayaga, G. C. Larsen, M. Kelly, and J. Mann, “Large-scale coherent turbulence structures in the atmospheric boundary layer over flat terrain,” *J. Atmos. Sci.* **79**, 3219–3243 (2022).

- ⁴J. Kaimal, J. Wyngaard, D. Haugen, O. Coté, Y. Izumi, S. Caughey, and C. Readings, “Turbulence structure in the convective boundary layer,” *J. Atmos. Sci.* **33**, 2152–2169 (1976).
- ⁵N. Hutchins, K. Chauhan, I. Marusic, J. Monty, and J. Klewicki, “Towards reconciling the large-scale structure of turbulent boundary layers in the atmosphere and laboratory,” *Boundary-Layer Meteorol.* **145**, 273–306 (2012).
- ⁶P. P. Sullivan and E. G. Patton, “The effect of mesh resolution on convective boundary layer statistics and structures generated by large-eddy simulation,” *J. Atmos. Sci.* **68**, 2395–2415 (2011).
- ⁷B. Jayaraman and J. G. Brasseur, “Transition in atmospheric boundary layer turbulence structure from neutral to convective, and large-scale rolls,” *J. Fluid Mech.* **913**, A42 (2021).
- ⁸M. Abkar and F. Porté-Agel, “Influence of atmospheric stability on wind-turbine wakes: A large-eddy simulation study,” *Phys. Fluids* **27**, 035104 (2015).
- ⁹W. El-Aaskary, I. Sakr, A. M. AbdelSalam, and M. Abuhegazy, “Modeling of wind turbine wakes under thermally-stratified atmospheric boundary layer,” *J. Wind Eng. Ind. Aerodyn.* **160**, 1–15 (2017).
- ¹⁰P. Moriarty, N. Bodini, L. Cheung, N. Hamilton, T. Herges, C. Kaul, S. Letizia, M. Pekour, and E. Simley, “Overview of recent observations and simulations from the American WAKE experiment (AWAKEN) field campaign,” *J. Phys.* **2505**, 012049 (2023).
- ¹¹L. Cheung, A. Hsieh, M. Blaylock, T. Herges, N. deVelder, K. Brown, P. Sakievich, D. Houck, D. Maniaci, C. Kaul, R. Rai, N. Hamilton, A. Rybchuk, R. Scott, R. Thedin, M. Brazell, M. Churchfield, and M. Sprague, “Investigations of farm-to-farm interactions and blockage effects from awaken using large-scale numerical simulations,” *J. Phys.* **2505**, 012023 (2023).
- ¹²L. Cheung, A. Hsieh, M. Blaylock, T. Herges, N. deVelder, K. Brown, P. Sakievich, D. Houck, D. Maniaci, C. Kaul, R. Rai, N. Hamilton, A. Rybchuk, R. Scott, R. Thedin, W. Radunz, P. Peixoto, and B. Carmo, “Model intercomparison for the AWAKEN king plains wind farm in idealized unstable and stable conditions,” Technical Report No. SAND2024-03828C (Sandia National Laboratories, 2023).
- ¹³A. Crespo, J. Hernandez, and S. Frandsen, “Survey of modelling methods for wind turbine wakes and wind farms,” *Wind Energy* **2**, 1–24 (1999).
- ¹⁴N. O. Jensen, *A Note on Wind Generator Interaction* (Risø National Laboratory, 1983).
- ¹⁵M. Bastankhah and F. Porté-Agel, “Experimental and theoretical study of wind turbine wakes in yawed conditions,” *J. Fluid Mech.* **806**, 506–541 (2016).
- ¹⁶A. Niayifaar and F. Porté-Agel, “Analytical modeling of wind farms: A new approach for power prediction,” *Energies* **9**, 741 (2016).
- ¹⁷J. F. Ainslie, “Calculating the flowfield in the wake of wind turbines,” *J. Wind Eng. Ind. Aerodyn.* **27**, 213–224 (1988).
- ¹⁸G. V. Iungo, V. Santhanagopalan, U. Ciri, F. Viola, L. Zhan, M. A. Rotea, and S. Leonardi, “Parabolic RANS solver for low-computational-cost simulations of wind turbine wakes,” *Wind Energy* **21**, 184–197 (2018).
- ¹⁹P. Bradstock and W. Schlez, “Theory and verification of a new 3D RANS wake model,” *Wind Energy Sci. Discuss.* **2020**, 1–15.
- ²⁰S. Letizia and G. V. Iungo, “Pseudo-2D RANS: A LiDAR-driven mid-fidelity model for simulations of wind farm flows,” *J. Renewable Sustainable Energy* **14**, 023301 (2022).
- ²¹L. A. Martinez-Tossas, J. King, E. Quon, C. J. Bay, R. Mudafort, N. Hamilton, M. F. Howland, and P. A. Fleming, “The curled wake model: A three-dimensional and extremely fast steady-state wake solver for wind plant flows,” *Wind Energy Sci.* **6**, 555–570 (2021).
- ²²M. P. van der Laan, M. Kelly, M. Baungaard, and A. Dicholkar, “A simple RANS inflow model of the neutral and stable atmospheric boundary layer applied to wind turbine wake simulations,” *Wind Energy Sci. Discuss.* **2024**, 1–17.
- ²³R. Krishnamurthy, R. K. Newsom, D. Chand, and W. J. Shaw, “Boundary layer climatology at ARM Southern Great Plains,” Technical Report No. PNNL-30832 [Pacific Northwest National Lab. (PNNL), Richland, WA, 2021].
- ²⁴B. D. Hirth, J. L. Schroeder, and J. G. Guynes, “Diurnal evolution of wind structure and data availability measured by the doe prototype radar system,” *J. Phys.* **926**, 012003 (2017).
- ²⁵K. Brown, L. Cheung, N. deVelder, T. Herges, A. Hsieh, M. Blaylock, G. Yalla, R. Knaus, D. Maniaci, and B. Hirth, “Estimating uncertainties from dual-

- Doppler radar measurements of onshore wind plants using LES,” *J. Phys.* **2767**, 092111 (2024).
- ²⁶M. A. Sprague, S. Ananthan, G. Vijayakumar, and M. Robinson, “Exawind: A multifidelity modeling and simulation environment for wind energy,” *J. Phys.* **1452**, 012071 (2020).
- ²⁷A. S. Almgren, J. B. Bell, P. Colella, L. H. Howell, and M. L. Welcome, “A conservative adaptive projection method for the variable density incompressible Navier–Stokes equations,” *J. Comput. Phys.* **142**, 1–46 (1998).
- ²⁸K. Sverdrup, N. Nikiforakis, and A. Almgren, “Highly parallelisable simulations of time-dependent viscoplastic fluid flow with structured adaptive mesh refinement,” *Phys. Fluids* **30**, 093102 (2018).
- ²⁹M. B. Kuhn, M. T. Henry de Frahan, P. Mohan, G. Deskos, M. Churchfield, L. Cheung, A. Sharma, A. Almgren, S. Ananthan, M. Brazell, L. A. Martinez-Tossas, R. Thedin, J. Rood, P. Sakievich, G. Vijayakumar, W. Zhang, and M. A. Sprague, “AMR-Wind: A performance-portable, high-fidelity flow solver for wind farm simulations,” *Wind Energy* (submitted).
- ³⁰A. Sharma, M. J. Brazell, G. Vijayakumar, S. Ananthan, L. Cheung, N. deVelder, M. T. Henry de Frahan, N. Matula, P. Mullooney, J. Rood, P. Sakievich, A. Almgren, P. S. Crozier, and M. Sprague, “Exawind: Open-source CFD for hybrid-RANS/LES geometry-resolved wind turbine simulations in atmospheric flows,” *Wind Energy* **27**, 225–257 (2024).
- ³¹L. Cheung, M. J. Brazell, A. Hsieh, S. Ananthan, G. Vijayakumar, and N. deVelder, “Computation and comparison of the stable Northeastern US marine boundary layer,” AIAA Paper No. AIAA 2021-0454, 2021.
- ³²C.-H. Moeng, “A large-eddy-simulation model for the study of planetary boundary-layer turbulence,” *J. Atmos. Sci.* **41**, 2052–2062 (1984).
- ³³S. J. Kline, W. C. Reynolds, F. A. Schraub, and P. W. Runstadler, “The structure of turbulent boundary layers,” *J. Fluid Mech.* **30**, 741–773 (1967).
- ³⁴Data Archive Portal, see <https://a2e.energy.gov/about/dap> (US Department of Energy Atmosphere to Elections Program, 2024).
- ³⁵C. Alinot and C. Masson, “k- ϵ model for the atmospheric boundary layer under various thermal stratifications,” *J. Sol. Energy Eng.* **127**, 438 (2005).
- ³⁶P. A. Durbin, “Near-wall turbulence closure modeling without ‘damping functions,’” *Theoret. Comput. Fluid Dyn.* **3**, 1–13 (1991).
- ³⁷W. P. Jones and B. E. Launder, “The prediction of laminarization with a two-equation model of turbulence,” *Int. J. Heat Mass Transfer* **15**, 301–314 (1972).
- ³⁸A. Celic and E. H. Hirschel, “Comparison of eddy-viscosity turbulence models in flows with adverse pressure gradient,” *AIAA J.* **44**, 2156–2169 (2006).
- ³⁹D. C. Wilcox, *Turbulence Modeling for CFD* (DCW Industries La Canada, CA, 1998), Vol. 2.
- ⁴⁰F. R. Menter, “Two-equation eddy-viscosity turbulence models for engineering applications,” *AIAA J.* **32**, 1598–1605 (1994).
- ⁴¹P. Spalart and S. Allmaras, “A one-equation turbulence model for aerodynamic flows,” in 30th Aerospace Sciences Meeting and Exhibit, 1992.